Nuclear Engineering and Technology 51 (2019) 996–1007

Contents lists available at ScienceDirect

Nuclear Engineering and Technology

journal homepage: www.elsevier.com/locate/net

Original Article

Development of multi-cell flows in the three-layered configuration of oxide layer and their influence on the reactor vessel heating

Ji-Won Bae, Bum-Jin Chung*

Department of Nuclear Engineering, Kyung Hee University, 1732 Deogyeong-daero, Giheung-gu, Yongin-si, Gyeonggi-do, 17104, Republic of Korea

ARTICLE INFO

Article history:
Received 5 November 2018
Received in revised form
6 January 2019
Accepted 2 February 2019
Available online 4 February 2019

Keywords:
Severe accident
In-vessel retention
Oxide layer
Three-layer configuration
Aspect ratio
Multi-cell flow
Analogy

ABSTRACT

We investigated the influence of the aspect ratio (H/R) of the oxide layer on the reactor vessel heating in three-layer configuration. Based on the analogy between heat and mass transfers, we performed mass transfer experiments to achieve high Rayleigh numbers ranging from 6.70×10^{10} to 7.84×10^{12}. Two-dimensional (2-D) semi-circular apparatuses having the internal heat source were used whose surfaces of top, bottom and side simulate the interfaces of the oxide layer with the light metal layer, the heavy metal layer, and the reactor vessel, respectively. Multi-cell flow pattern was identified when the H/R was reduced to 0.47 or less, which promoted the downward heat transfer from the oxide layer and possibly mitigated the focusing effect at the upper metallic layer. The top boundary condition greatly affected the natural convection of the oxide layer due to the presence of secondary flows underneath the cold light metal layer.

1. Introduction

A hypothetical severe accident in the nuclear power plant accompanies the fuel melting. The heat load to the reactor vessel due to the decay heat and sensible heat of the corium may threaten the integrity of the reactor vessel. The IVR-ERVC (In-Vessel Retention of molten corium by the External Reactor Vessel Cooling) is a strategy to guarantee the integrity of the reactor vessel by retaining the corium inside the vessel by flooding the reactor cavity. If successful, it is the desirable strategy as it blocks any possibilities of the serious problems that may arise if the fission products release to the containment environment [1]. Thus it receives much attention [2,3].

The technical concern for the adoption of the IVR-ERVC is whether the cooling by ERVC exceeds the head load on the reactor vessel imposed by the molten corium. This strategy is adopted by nuclear power plants having a small power less than 1000 MWe such as the AP1000 of the Westinghouse. For larger power reactors such as EPR of 1800 MWe, the core-catcher is adopted as the reliability of the IVR is low due to smaller surface-to-volume ratio. Thus, the experimental verification and the phenomenological studies are still needed to explore the applicability of the IVR-ERVC strategy to middle and large power reactors including the APR1400 [4,5].

When the core melts are retained in the reactor vessel lower head, they are stratified into two- or three-layer configurations depending on the accident scenarios as shown in Fig. 1. In the three-layer configuration, the thickness of top light metal layer is reduced due to the formation of the additional heavy metal layer at the bottom, which has the potential to intensify the heat focusing to the reactor vessel through the thin light metal layer [5–7]. Thus, the three-layer configuration is worse than two-layer one. However, only a few studies have been conducted for the three-layer stratification and the phenomenological analysis was not enough, as the possibility of the three-layer configuration was recently raised by the MASCA experiment [8].

This study is the extension of the preceding study on the three-layer configuration [9] suggesting the formation of multi-cell flow in very shallow oxide layer. It lacks the detailed analysis about the influence of the multi-cell flow on the variation of upward and downward heat transfers and the certain range of aspect ratios (H/R) that multi-cell flows are formed. Therefore, we extended the same experiments to smaller aspect ratios (H/R) than that the formation of multi-cell flow was found in the preceding study [9] and measured the detailed local average heat transfers using carefully

* Corresponding author.
E-mail address: bjchung@khu.ac.kr (B.-J. Chung).

https://doi.org/10.1016/j.net.2019.02.004

Nomenclature

A	Area $[m^2]$
C	Molar concentration $[kmole/m^3]$
D_m	Mass diffusivity $[m^2/s]$
Da_H	Damkőhler number $(q'''H^2/k\Delta T)$
F	Faraday constant [94,485 × 10^3 C/$kmole$]
G	Gravitational acceleration [9.8 m/s^2]
Gr_H	Grashof number $(g\beta\Delta TH^3/\nu^2)$
H	Height $[m]$
h_h	Heat transfer coefficient $[W/m^2 \cdot K]$
h_m	Mass transfer coefficient $[m/s]$
$h^{*\|}$	Normalized heat transfer coefficient (h_h/q'''^{x})
I	Electric current $[A]$
I'''	Current per volume $[A/m^3]$
I_{lim}	Limiting current density $[A/m^2]$
K	Thermal conductivity $[W/m \cdot K]$
N	Number of electrons in charge transfer reaction
Nu_H	Nusselt number (h_hH/k)
Pr	Prandtl number (ν/α)
Q	Heat quantity $[W]$
Q^*	Normalized heat quantity $[W]$
Q	Heat generation rate $[W]$
q'''	Volumetric heat generation rate $[W/m^3]$
R	Radius corresponding to pool $[m]$
R_e	Equivalent radius corresponding to pool volume $[m]$
Ra_H	Rayleigh number $(g\beta\Delta TH^3/\alpha\nu)$
Ra'_H	Modified Rayleigh number (Ra_HDa_H)
Sc	Schmidt number (ν/D_m)
Sh_H	Sherwood number (h_mH/D_m)
T	Temperature $[K]$
t_{Cu}^{2+}	Transference number of Cu^{2+}
U_x	Uncertainty of x
W	Width of 2-D test rig $[m]$
X	Normalization factor

Greek symbols

A	Thermal diffusivity $[m^2/s]$
B	Volume expansion coefficient $[1/K]$
Γ	Dispersion coefficient
M	Viscosity $[kg/m \cdot s]$
N	Kinematic viscosity $[m^2/s]$
P	Density $[kg/m^3]$

Subscripts

B	Bulk
Bottom	Bottom plate
Dn	Downward
H	Heat transfer system
m	Mass transfer system
sd	Sideward
side	Side wall
top	Top plate
tot	Total
up	Upward

designed piecewise electrodes. This study focused on the reactor vessel heating by natural convection of corium stabilized in final configuration and did not deal with the transition phenomena such as crust formation.

Mass transfer experiments were conducted using copper sulfate-sulfuric acid ($CuSO_4$–H_2SO) electroplating system based on the analogy concept. With this, the idealized thermal boundary conditions without heat leakage to the environments were maintained and the high Ra'_H of the oxide layer was attained with compact apparatus. The Ra'_H ranged from 6.70 × 10^{10} to 7.84 × 10^{12}. The oxide layer of the three-layer configuration was simulated by the 2-D semi-circular facility called MassTER-OP2(HML) (Mass Transfer Experimental Rig for a 2-D Oxide Pool with Heavy Metal Layer), whose top plate, bottom plate and side wall simulate the interfaces with the light metal layer, the heavy metal layer, and reactor vessel, respectively.

2. Theoretical backgrounds

2.1. Phenomena in molten corium

In a severe accident, the molten core stratifies into either two- or three-layer configurations. In the case of the two-layer configuration, the upper layer contains metallic materials such as Fe and Zr and the lower layer consists of oxidized materials such as UO_2 and ZrO_2 (Fig. 1(a)). When there is enough unoxidized Zr in the upper metal layer, the U existed in the lower oxide layer migrates to the upper layer to form a heavy alloy. As the density of the alloy exceeds that of oxide layer, an additional heavy metal layer is formed under the oxide layer as shown in Fig. 1(b) so called the layer inversion. This three-layer configuration was recently demonstrated by MASCA experiments [8].

The oxide layer containing radioactive fission products generates decay heat continuously. The heat load imposed on the reactor

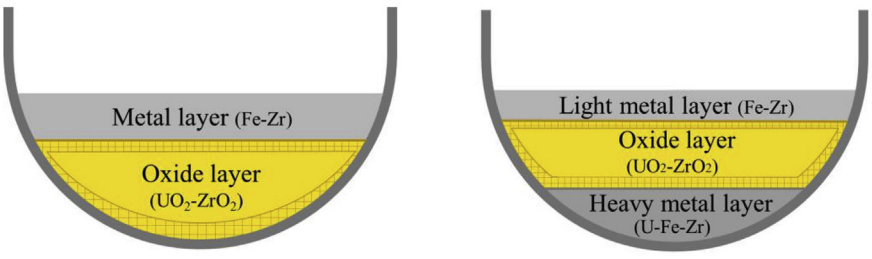

(a) Two-layer configuration (b) Three-layer configuration

Fig. 1. Layer compositions according to the configuration type.

vessel due to the natural convection of the oxide layer and the resulting heat transfers, is of prime concern threatening the integrity of the reactor vessel. The natural convection in this layer is special as the media contains the internal heat sources. To consider the volumetric heat generation (q'''), the modified Rayleigh number (Ra'_H) is defined by multiplying conventional Rayleigh number (Ra_H) and Damkőhler number (Da_H) [10,11]. The Da_H is the dimensionless parameter which converts the temperature difference (ΔT) into the volumetric heat generation (q'''). Thus, the Ra'_H is expressed as

$$Ra'_H = Ra_H \times Da_H = \frac{g\beta\Delta T H^3}{\alpha\nu} \times \frac{q''' H^2}{k\Delta T} = \frac{g\beta q''' H^5}{\alpha\nu k}, \quad (1)$$

where

$$Da_H = \frac{q''' H^2}{k\Delta T}. \quad (2)$$

The light metal layer does not contain an internal heat source. Instead, it transfers the heat from the oxide layer to the reactor vessel especially when the upper side is not cooled effectively by the coolant. Due to the thin metallic layer, the heat focusing to the reactor vessel becomes important. In the three-layer configuration, as the light metal layer is thinner than that in two-layer configuration due to the loss of heavy metal composition to form the additional heavy metal layer, the heat focusing to the reactor vessel is intensified.

Fig. 2 shows the flow patterns of oxide layer in the three-layer configuration. The natural convective downward flows are developed by the cooling along the side wall. They merge at the center of the lower surface. Then they rise upward and disperse towards the edges of the upper surface, forming the main flow having a twin-cell shape. The pattern of main flow varies depending on the aspect ratio (H/R) of the oxide layer. Natural convective flows are formed underneath the upper surface called secondary flow. Stagnant flows are generated at the edges where the lower surface and the side wall are in contact. Kim and Chung [9] reported that as the oxide layer becomes shallow, the number of cells increase and form a multi-cellular flow.

2.2. Previous studies

Table 1 summarizes the existing studies about the natural convection of the oxide layer in the two- and the three-layer configurations. There are many studies for the two-layer configuration, whereas studies about three-layer configuration are rare as its possibility is recently discovered.

2.2.1. Two-layer experiments

Bonnet and Seiler [12] investigated the heat transfer influences of the natural convection in the oxide pool on the reactor vessel. They used a 2-D (2-Dimensional) semi-circular facility (BALI) with cellulose added water as the working fluid. The volumetric heating was obtained by joule heating. They reported that there are three different zones in the oxide layer, an upper unstable layer with uniform temperature, a lower stratified zone in temperature, and a boundary layer. The angular heat flux decreased toward the bottom as the thermal boundary layer developed along the curved wall, and its profiles depended on the top boundary condition. The heat transfer correlations for 2-D geometry were developed for Ra'_H ranging from 10^{13} to 10^{17}.

$$Nu_{up} = 0.383 {Ra'_H}^{0.233} \quad (3)$$

and

$$Nu_{dn} = 0.116 {Ra'_H}^{0.25} \quad (4)$$

Lee et al. [13] conducted experiments with a 2-D semi-circular pool (SIGMA CP) for Ra'_H of 10^6–10^{11}. Four thin cable-type heaters were used to simulate continuously generated decay heat in the pool. The working fluids were air and water, which corresponded to Pr of 0.7 and 4 to 8, respectively. Regardless of the type of working fluid, the heat transfer to side wall was increased with the increase of the angle measured from the bottom. The heat flux to the upper section of the side wall was greater for the top adiabatic cases than the top isothermal cases because the internal heat transfers to the upper side wall rather than top surface. They proposed the correlations.

$$Nu_{up} = 0.31\left(Ra'_H Pr^{-0.36}\right)^{0.245} \quad (5)$$

and

$$Nu_{dn} = 0.219\left(Ra'_H Pr^{-0.215}\right)^{0.235} \quad (6)$$

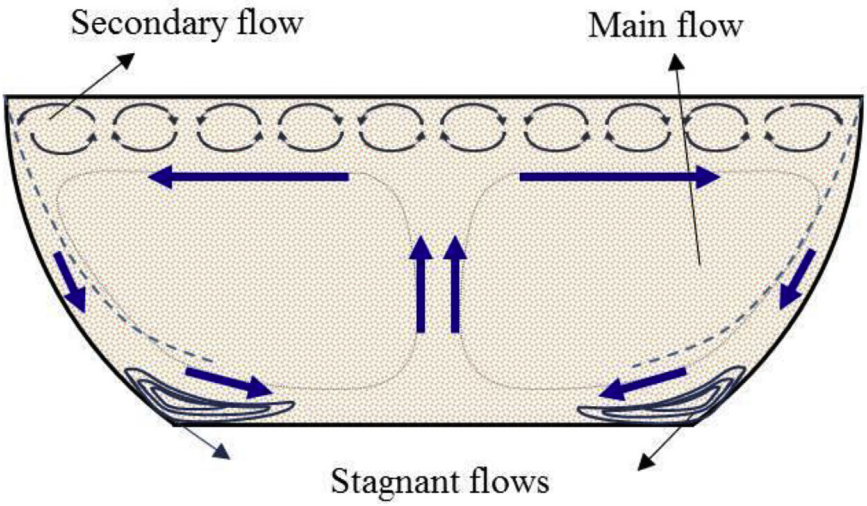

Fig. 2. Flow patterns of the oxide layer in three-layer configuration.

Table 1
Summary of previous studies.

	Facility	Oxide pool shape (Dimension)	Working fluid	Ra'_H	Pr	Correlations
2-Layer	BALI	Semicircle (2-D)	Cellulose added water	10^{13}–10^{17}	≈7	$Nu_{up} = 0.383Ra'^{0.233}_H$ $Nu_{dn} = 0.116Ra'^{0.25}_H(H/R_e)^{0.32}$
	SIGMA CP	Semicircle (2-D)	Air and Water	5×10^6–7×10^{11}	0.7; 4 - 8	$Nu_{up} = 0.31(Ra'_H Pr^{-0.36})^{0.245}$ $Nu_{dn} = 0.219(Ra'_H Pr^{-0.215})^{0.235}$
	ACOPO	Hemisphere (3-D)	Freon-113 and Water	1×10^{12}–2×10^{16}	≈7	$Nu_{up} = 1.95Ra'^{0.18}_H$ $Nu_{dn} = 0.3Ra'^{0.22}_H$
	UCLA	Hemisphere (3-D)	Freon-113	4.7×10^{11}–8×10^{13}	8.2–9.5	$Nu_{dn} = 0.54Ra'^{0.2}_H(H/R_e)^{0.25}$
	MassTER-OP2	Semicircle (2-D)	Copper sulfate − sulfuric acid	4.55×10^{12}–8.99×10^{14}	2014	$Nu_{up} = 1.046Ra'^{0.211}_H$
	MassTER-OP3	Hemisphere (3-D)		8.64×10^{12}–1.46×10^{15}		$Nu_{dn} = 0.27Ra'^{0.209}_H$
3-Layer	SIMECO	Chopped semicircle (2-D)	Water	6.01×10^{12}–8.7×10^{12}	≈7	-
	MassTER-OP2 (HML)	Chopped semicircle (2-D)	Copper sulfate − sulfuric acid	5.24×10^{10}–4.30×10^{13}	2014	-

*2-D, two-dimensional, 3-D, three-dimensional.

Theofanous et al. [14] simulated the oxide pool in the 3-D (3-Dimensional) hemi-spherical facility (ACOPO) filled with Freon-113 or Water. The scale of facility was 1/2 of AP600 with the diameter of 2 m. The Ra'_H was varied from 1×10^{12} to 2×10^{16}. To simulate the internal heat source, they preheated the working fluids and interpreted the transient state as quasi-stationary natural convection state. The angular heat flux at the curved surface decreased from the upper to the lower section. They developed the correlations for 3-D geometry.

$$Nu_{up} = 1.95{Ra'}_H^{0.18} \tag{7}$$

and

$$Nu_{dn} = 0.3{Ra'}_H^{0.22} \tag{8}$$

Asfia and Dhir [15] carried out the experimental study for the natural convection heat transfer in 3-D hemi-spherical pool (UCLA), varying the diameters (0.43 m, 0.6 m) and the top boundary conditions (cooling, insulation). The Freon-113 was used as working fluid and was uniformly heated by microwave to simulate the decay heat in the pool. The Ra'_H ranged from 4.7×10^{11} to 8×10^{13}. They reported that whether the top boundary condition was cooling or insulation, it had little influence on the heat transfers in the pool. They also observed that the angular heat flux increased until 80°–90° section and then decreased slightly. The experimentally developed correlation is

$$Nu_{dn} = 0.54{Ra'}_H^{0.2}(H/R_e)^{0.25} \tag{9}$$

Kim and Chung [16], Park and Chung [17] and Kim et al. [18] performed the mass transfer experiments using the 2-D semi-circular and 3-D hemi-spherical facilities (MassTER-OP2 and MassTER-OP3). The copper sulfate-sulfuric acid solution was used as working fluid. The range of Ra'_H was 4.55×10^{12}–1.46×10^{15}. They investigated the natural convection of the oxide pool in the two-layer configuration varying the sizes of oxide pool and the shapes of internal heat source simulated by copper anode. They also reported that, in general, an increase in Ra'_H leads to an increase in Nu, but the angular variations of heat flux were not affected by Ra'_H in the 2-D oxide pool of two-layer configuration. All results of them shows that the angular Nu at the curved wall increased with the angle measured from the bottom and had a peak value at the uppermost section. The shape of internal heat source did not affect the Nu measured at the lower curved wall, but the Nu measured from the top surface showed a large difference depending on the shape of heat source. It was because the friction due to the internal heat source structure disturbed the upward flow induced by the buoyant force. This disturbance was greater in 3-D results. They also established the correlations.

$$Nu_{up} = 1.046{Ra'}_H^{0.211} \tag{10}$$

and

$$Nu_{dn} = 0.27{Ra'}_H^{0.209} \tag{11}$$

2.2.2. Three-layer experiments

Segal et al. [19] carried out the integral experiments and simulated three-layer configuration with a 2-D semi-circular facility (SIMECO) using paraffin oil (upper layer), water (middle layer) and chlorobenzene (lower layer). The heights (H) of them were 5 cm, 18 cm and 4 cm, respectively. The heater was located at 4 cm - 24 cm from the bottom and supplied heat to entire middle layer and part of the upper layer. The Ra'_H varied from 6.01×10^{12} to 8.7×10^{12}. The angular heat flux increased with the angle from the bottom and had a maximum value at the middle of the oxide layer. This differs from the results of other existing studies [12–17] where the maximum value appeared at uppermost section of the oxide layer. Therefore, it does not account for the focusing effect at the upper metal layer.

Kim et al. [20] conducted the mass transfer experiments to investigate the natural convection phenomena in oxide layer of the three-layer configuration and compare with two-layer configuration. They simulated stratified oxide layer of the three-layer configuration with 2-D semi-circular MassTER-OP2(HML) with chopped bottom (Mass Transfer Experimental Rig for a 2-D Oxide Pool with Heavy Metal Layer). The radius (R) was 0.1 m and width (W) was 0.04 m. The height (H) was 0.0565 m corresponding to aspect ratio (H/R) of 0.56, which was determined by the code calculation results in Park et al. [5]. The Ra'_H ranged from 1.49×10^{12} to 1.36×10^{13}. They reported that the heat load on the light metal layer and uppermost curved wall of the three-layer configuration was higher than that of the two-layer configuration, which suggests that in terms of focusing effect, the three-layer configuration is more conservative than two-layer configuration.

Kim and Chung [9] analyzed the effect of the aspect ratio (H/R) on the natural convection heat transfer in the oxide layer through the experimental study. The heights (H) of MassTER-OP2(HML) varied to three: 0.028 m, 0.056 m and 0.078 m, which correspond the Ra'_H from 5.24×10^{10} to 4.30×10^{13}. They concluded that the ratios of upward heat to total heat (Q_{up}/Q_{tot}) in the oxide layer of the three-layer were higher than those for two-layer, which means the heat focusing to the vessel at the light metal layer was intensified in the three-layer configuration. Their study confirmed the formation of multi-cell flows when the aspect ratio (H/R) was 0.28. However, it is not certain whether the similar multi-cell flows are formed at larger aspect ratios. Also the stronger evidence of multi-cell flow patterns should be accumulated by more experiments.

3. Experiments

3.1. Experimental methodology

Heat and mass transfers are analogous as they are expressed mathematically the same. Thus their governing parameters are matched as shown in Table 2 [21], which means that heat transfer problems can be solved by mass transfer experiments, and vice versa [22].

In this study, the copper sulfate-sulfuric acid ($CuSO_4$–H_2SO_4) electroplating system was utilized as the mass transfer system. When the electric potential is applied, cupric ions are generated at the anode and are transferred to the cathode by convection, diffusion and electrical migration. The transferred cupric ions are reduced at the cathode, resulting in large density decrease of the solution near the cathode which enables the achievement of the high buoyant force with the compact test apparatus. Also, the amount of transferred cupric ions, simulating the transferred heat, can be measured easily by the electric currents. In order to minimize the electric migration, which does not exist in the heat transfer system, the sulfuric acid was added to increase the electric conductivity of the solution to reduce the establishment of electric field. The physical properties of the bulk fluid were determined using several equations provided by Fenech and Tobias [23].

To calculate the mass transfer coefficient (h_m), we should know the current density and concentration of the cupric ions at the cathode and the bulk. However, the concentration of cupric ions near the cathode is difficult to measure. Thus, the limiting current technique was used. When the applied voltage increases, the current between the two electrodes increases initially. And then it reaches a plateau where the increase in the applied voltage does not increase the current. This is because the transfer of cupric ions no more increases as the reduction process of copper ions is faster than the transport process of them to the cathode. At this stage, the concentration of copper ions at the cathode can be regarded as zero. This constant current is limiting current. Thus, at the limiting current condition, the mass transfer coefficient (h_m) can be determined by the limiting current density I_{lim} and the bulk concentration C_b only. The total mass transfer flux is I_{lim}/nF. The mass transfer flux contributed by the electrical migration is given by $t_{Cu^{2+}}I_{lim}/nF$, which should be removed from the total mass transfer flux as it does not appear in the heat transfer system. The mass transfer coefficient including the limiting current is

$$h_m = \frac{(1 - t_{Cu^{2+}})I_{\lim}}{nFC_b} \tag{12}$$

By the analogy between heat and mass transfers, the Damkőhler number for mass transfer system can be expressed as

$$Da_m = \frac{(1 - t_{Cu^{2+}})I'''H^2}{nFD_m\Delta C} \tag{13}$$

where the volumetric electric current (I'''), mass diffusivity (D_m) and copper sulfate concentration difference (ΔC) corresponds to the volumetric heat generation rate (q'''), thermal conductivity (k) and temperature difference (ΔT), respectively.

Finally, the Ra'_H for the mass transfer system is defined as follows:

$$Ra'_H = \left(\frac{gH^3\Delta\rho}{D_m\nu\rho} \times \frac{127.5\Delta C}{\Delta\rho}\right) \times \left(\frac{(1 - t_{Cu^{2+}})I'''H^2}{nFD_m\Delta C}\right) = 127.5\frac{(1 - t_{Cu^{2+}})gI'''H^5}{nFD_m^2\nu\rho} \tag{14}$$

Where,

$$\frac{\Delta\rho}{C_{Cu^{2+}}} = \frac{\Delta\rho}{\Delta C} \sim 127.5 \tag{15}$$

Table 2
Corresponding governing parameters of heat and mass transfer systems.

Heat transfer system	Mass transfer system
$Pr = \frac{\nu}{\alpha}$	$Sc = \frac{\nu}{D}$
$Nu_H = \frac{h_h H}{k}$	$Sh_H = \frac{h_m H}{D_m}$
$Ra_H = \frac{g\beta\Delta TH^3}{\alpha\nu}$	$Ra_H = \frac{gH^3}{D_m\nu}\frac{\Delta\rho}{\rho}$

3.2. Experimental apparatus

Fig. 3 indicates the MassTER-OP2(HML). The radius (R) was 0.1 m and the width (W) was 0.04 m, which are the same as those of MassTER-OP2 [16,20]. The heights (H) were ranged to 0.028 m, 0.038 m and 0.047 m to simulate the shallow oxide layers, which were determined to be between 0.028 m and 0.056 m to explore the range of aspect ratios resulting multi-cell flows. 0.056 m was the calculated height of oxide pool by Park et al. [5] for APR1400 causing the twin-cell flow and 0.028 m was the height we observed the multi-cell flow in the preceding study [9].

The interfaces between the light metal layer, the heavy metal layer, and reactor vessel and the oxide layer were simulated into the top plate, the bottom plate and the side wall, respectively. Each of the top, bottom and side surfaces was composed of the cathode copper plate. The halves of top, bottom and side surfaces were single electrodes. The other halves were piecewise electrodes divided into 8, 8, and 4 electrodes, respectively, so as to measure the local average heat transfers. Each of the electrodes was insulated by thin insulating layers. In order to simulate the internal heat sources, the trapezium anode coppers attached at the both front and rear side plates [20]. The apparatus was filled with the aqueous solution of copper sulfate–sulfuric acid ($CuSO_4$–H_2SO_4).

For the electroplating system, the currents are measured at cathode. The anode is improper for measurement as $CuSO_4$ crystal is deposited at the surface [24]. The upward natural convective flows are formed at the cathode surfaces as copper ions reduced at the cathode causing the decrease of fluid density.

However, in the IVR phenomena, the downward natural convective flows are developed along the side wall by the ERVC system as shown in Fig. 2. In order to simulate the downward flows toward the bottom with the electroplating system, the direction of gravity has to be reversed. Thus, the experiments were conducted at the inverted arrangement as shown in Fig. 4 in line with the earlier studies [16,25].

Fig. 4 also shows the test circuit. The electric potential was applied by the power supply (K1205D of VüPower). The measured current signals at each cathode and the applied voltages were monitored by data acquisition system (DAQ) (NI-9227 of National Instruments, 34972A of Agilent, respectively) and recorded on LABVIEW program.

3.3. Test matrix

Table 3 presents the thermal boundary conditions for experiments. For all the aspect ratios (H/R) of 0.28, 0.38 and 0.47, the tests were performed for both isothermal and adiabatic boundary conditions of top and bottom plates. The side wall was maintained in

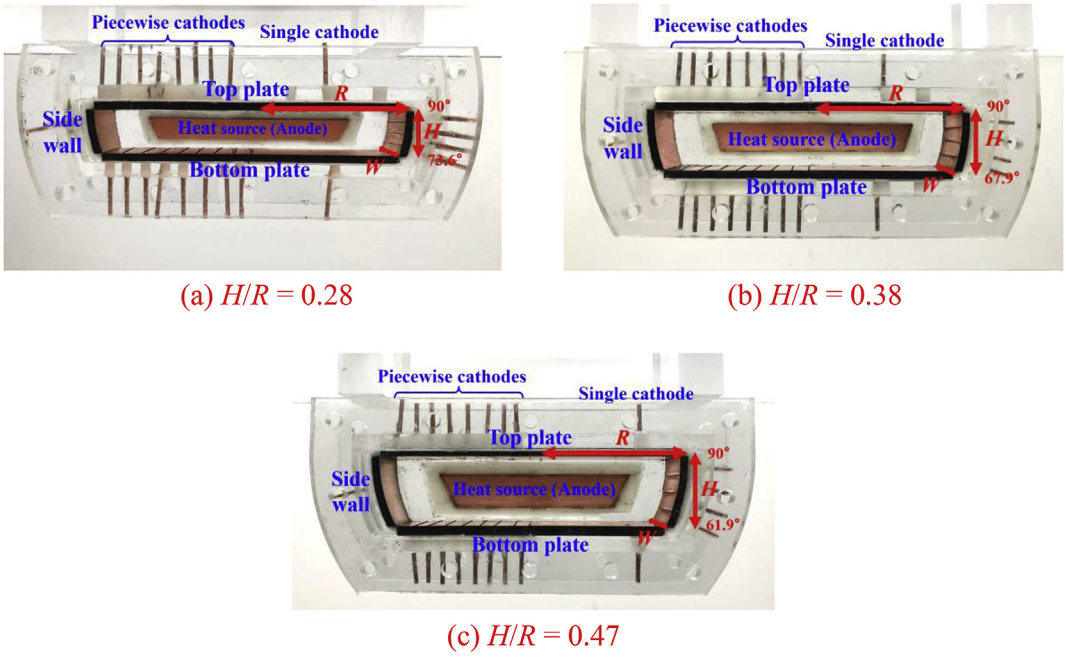

Fig. 3. Experimental apparatus.

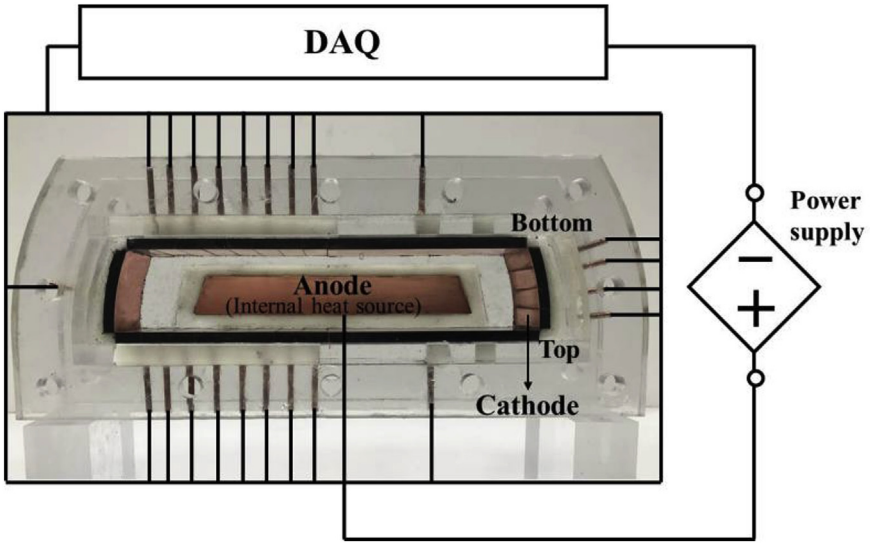

Fig. 4. Test circuit.

the isothermal condition in all cases. These conditions were set up as the extreme cooling situations. The top insulating condition is a hypothetically conservative case when the heat transfer to the light metal layer does not occurs. And the bottom insulating condition is another conservative case when the heavy metal layer consists of a lot of fission products, generating the decay heat excessively. The actual conditions in a severe accident will lie in between these extrema.

Table 3
Boundary conditions for experiments.

	Thermal boundary condition		
	Side	Top	Bottom
Case 1	Isothermal	Isothermal	Isothermal
Case 2			Adiabatic
Case 3		Adiabatic	Isothermal
Case 4			Adiabatic

Table 4 shows the test matrix of this study. The range of Ra'_H was 6.70×10^{10}–7.84×10^{12}, which is smaller than Ra'_H in the oxide pool of the two-layer configuration ranging from 10^{15} - 10^{17} as the Ra'_H is greatly affected by height of the oxide pool (H) as shown in Eq. (1). Also for the current range of Ra'_H, even though there may be reduction in driving force, similar thermal hydraulic behaviors are expected. The Sc corresponding the Pr in heat transfer system was 2,014, which was also determined by the concentrations of $CuSO_4$ (0.05 M) and H_2SO_4 (1.5 M). Discussions were made on the phenomenological bias the high Pr is caused.

Table 4
Test matrix.

H/R	Case	Decay heat (q''')	Ra'_H	Pr (Sc)
0.28	Case 1	3512 A/m^3	9.72×10^{11}	2014
	Case 2	3094 A/m^3	8.57×10^{11}	
	Case 3	364 A/m^3	1.10×10^{11}	
	Case 4	242 A/m^3	6.70×10^{10}	
0.38	Case 1	2122 A/m^3	2.37×10^{12}	
	Case 2	1973 A/m^3	2.20×10^{12}	
	Case 3	313 A/m^3	3.49×10^{11}	
	Case 4	245 A/m^3	2.74×10^{11}	
0.47	Case 1	1913 A/m^3	7.84×10^{12}	
	Case 2	1844 A/m^3	7.56×10^{12}	
	Case 3	258 A/m^3	1.06×10^{12}	
	Case 4	203 A/m^3	8.30×10^{11}	

Table 5
Current differences between one-piece and piecewise electrodes.

		Side wall	Top plate	Bottom plate
$H/R = 0.28$	Case 1	−5.89%	−1.23%	7.57%
	Case 2	−1.30%	−5.34%	–
	Case 3	0.21%	–	6.23%
	Case 4	−2.57%	–	–
$H/R = 0.38$	Case 1	2.88%	−1.43%	4.36%
	Case 2	5.33%	−1.86%	–
	Case 3	6.21%	–	5.06%
	Case 4	3.24%	–	–
$H/R = 0.47$	Case 1	7.52%	5.18%	1.04%
	Case 2	−6.36%	4.94%	–
	Case 3	3.00%	–	7.26%
	Case 4	2.08%	–	–

※ $\frac{I_{one-piece} - \sum I_{piecewise}}{I_{one-piece}} \times 100(\%)$.

3.4. Uncertainty analysis

The uncertainties of the mass transfer experiments were analyzed by the data reduction equations [26]. The final dependent variable is the mass transfer coefficient (h_m) and its uncertainty can be expressed as:

$$h_m = f(t_{Cu^{2+}}, I_{\lim}, C_b) \Rightarrow h_m = \frac{(1 - t_{Cu^{2+}})I_{\lim}}{nFC_b}$$

and

$$U_{h_m}^2 = \left(\frac{\partial h_m}{\partial t_{Cu^{2+}}} U_{t_{Cu^{2+}}}\right)^2 + \left(\frac{\partial h_m}{\partial I_{\lim}} U_{I_{\lim}}\right)^2 + \left(\frac{\partial h_m}{\partial C_b} U_{C_b}\right)^2 \quad (16)$$

The uncertainties of $t_{Cu^{2+}}$, I_{lim} and C_b are further estimated as the same way with Eq. (16) until the basic measurement quantities remain such as electric current, length and masses of $CuSO_4$ and H_2SO_4. The measurement errors of the electric current, the length and the mass were assumed to be the halves of their minimum scales. Therefore, the measurement errors in electric current, length and mass were 2.38×10^{-7} A, 2.5×10^{-5} m and 5×10^{-7} kg, respectively. The fractional uncertainties of each tests on three different aspect ratios (H/R) were 0.76% ($H/R = 0.28$), 0.59% ($H/R = 0.38$) and 0.65% ($H/R = 0.47$), which shows the accuracy of the experimental technique.

4. Results and discussion

4.1. Reliability of the piecewise electrodes

In order to check the influence of the very thin insulating layers between piecewise electrodes, we compared the electric currents measured by one-piece electrode in the half surface and the sum of the electric currents measured by piecewise electrodes in the other half surface for each surface. Table 5 indicates the relative differences of the electric currents between one-piece electrode and sum of piecewise electrodes. They were within 8% in all cases. We concluded that the influences of insulating layers between piecewise electrodes are not very significant.

4.2. Normalization of the measured results

The Ra'_H, which is the dominant factor for Nu_H, consists of volumetric decay heat (q'''), height (H) and fluid properties as shown in Eq. (1). In the current experimental system using limiting current technique, the limiting current, which corresponds to decay heat, is determined by the experimental conditions and is not a control variable. As shown in Table 4, the decay heats were varied case by case.

In order to compare the test results with different limiting current densities and to focus on the influence of the height, the normalization with the volumetric heat generation rate was needed to achieve generalized expression for arbitrary heating conditions while maintaining the phenomenological similarity. Thus the empirical heat transfer correlations of Steinberner and Reineke [27] were used as shown in Table 6, which were developed with the existence of the internal heat source for the rectangular enclosure with all sides cooled. It was derived in the range of $5 \times 10^{12} < Ra'_H < 3 \times 10^{13}$ and a Prandtl number of 7, which are similar conditions for the current experiments. In the correlation for the side wall, the Nu_H is proportional to the Ra'_H to the power of 0.19. Since q''' is included within the Ra'_H, we divided the heat transfer coefficient (h_h) by q''' to the power of 0.19 and then obtained the normalized heat transfer coefficient (h^*). The top and the bottom plates were normalized the same way.

4.3. Comparison of local heat transfer

4.3.1. Influence of aspect ratio on local heat transfer

For the three-layer configuration of molten corium, the height (H) of oxide layer affects the flow patterns in the oxide layer and resulting heat transfer on each interface. In the aspect of heat transfer, as the H of the oxide layer decreases, the cooling by the side wall decreases, resulting in two conflicting phenomena of either impairing or enhancing the heat transfer. The reduced driving force either impairs the heat transfer by weaken the main flow or enhances the heat transfer by forming multi-cell flows, which enhance the heat exchange between the top and bottom plates. The multi-cell flow pattern envisages as shown in Fig. 5 [28]. For the high Pr, due to the very thin thermal boundary layer, the configuration of cell flow would be faint [30]. However, due to the thicker momentum boundary layer than thermal one ($\delta_T < \delta$), the less cooled fluid is entrained from the bottom toward the top surface and upward heat transfer is enhanced [18].

The multi-cell flow also appears in the Rayleigh-Bénard convection occurring at the shallow enclosure with bottom heating and top cooling condition [22,28,29]. The current study differs from the Rayleigh-Bénard convection by the existence of volumetric heat source and the additional side wall cooling. For the side cooling case, the driving force of natural convection is mainly generated along the side walls. When the side wall cooling decreases due to the reduced height (H), the weaken downward flows weaken the driving force for the main flow and they do not reach the center, leading the ascending plumes at the midway. Then they interact with descending plumes and the symmetrical multi-cell flow is formed. The formation of the multi-cell flow can be observed as the

Table 6
Normalization for the top plate, the side wall and the bottom plate.

	Side wall	Top plate	Bottom plate
Correlations [27]	$Nu_{sd} = 0.85{Ra'}_H^{0.19}$	$Nu_{up} = 0.345{Ra'}_H^{0.233}$	$Nu_{dn} = 1.389{Ra'}_H^{0.095}$
Normalization factor (x)	0.19	0.233	0.095
Normalized value	$h/{q'''}^{0.19}$	$h/{q'''}^{0.233}$	$h/{q'''}^{0.095}$

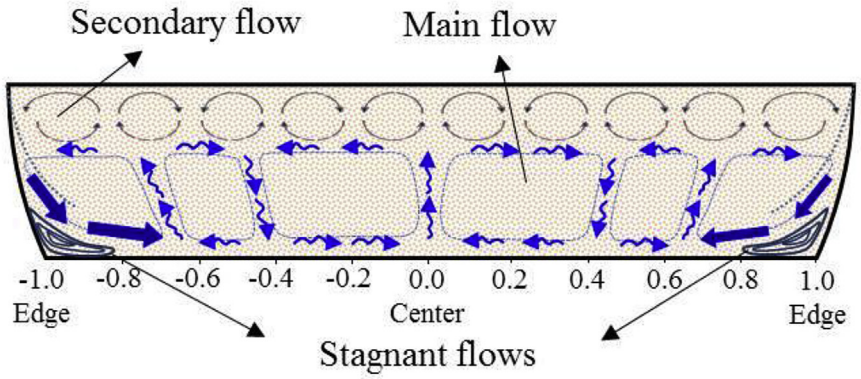

Fig. 5. Multi-cell flow in the oxide layer of three-layer configuration.

results of heat distribution on the bottom plate.

Fig. 6 presents the normalized local heat transfer coefficients at the bottom plate (h^*_{bottom}) measured at all isothermal condition for three different aspect ratios (H/R). The position of bottom plate from the center to edge is normalized by 0–1 for comparison as the length from center to edge is different for each test apparatus. h^*_{bottom}'s were highest at the center and reduced toward the edge. They have two inflection points near position 0.425 and 0.625, which are evidences of the multi-cell flow formation. For the bottom plate, the reduced height (H) meaning the cooling length causes the decrease of the driving force for the main flow. Thus, in shallow oxide layer as shown in Fig. 5, the ascending and descending plumes are formed and the inflection points appear as the flows merge and disperse, respectively. Since the trends of all results are similar, it is obvious that multi-cell flow was formed within the oxide layer for $0.28 \leq H/R \leq 0.47$.

The normalized heat transfer coefficients at the bottom (h^*_{bottom}) are similar for 0.47 and 0.38. But, they increase relatively large as the H/R decreases to 0.28. As explained above, there are competition of two phenomena according to the decrease of the H/R: the degradation of the heat transfer due to the reduced driving force for natural convection and the enhancement of heat transfer due to the less cooled, hotter flows moving toward the bottom plate. For H/R's of 0.38 and 0.47, the impairment and the enhancement seem to be similar and the normalized heat transfer coefficients almost coincide although the H/R decreases from 0.47

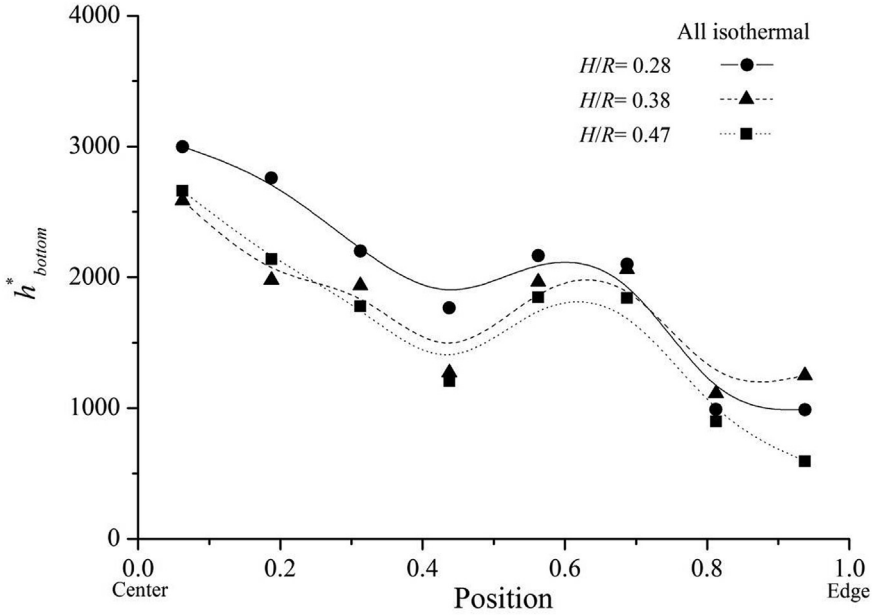

Fig. 6. Downward normalized heat transfer coefficients according to aspect ratios.

to 0.37. However, when the H/R is sufficiently shallow as 0.28, the enhancement of heat transfer seems to be dominant. From the position near 0.625 to the edge of bottom plate, the heat transfer behaviors for H/R are different due to the formation of the stagnant flows as shown in Fig. 5.

Fig. 7 shows the normalized local heat transfer coefficients for the top plate (h^*_{top}) for three different aspect ratios (H/R). h^*_{top}'s are much higher than h^*_{bottom} due to the additional secondary natural convective flows shown in Fig. 5. The heat transfers are reduced with the decrease of H/R from 0.47 to 0.38 but increased as the H/R decreases further to 0.28. As in the bottom plate, there is also the competition of two phenomena in the top plate: the impairment of heat transfer due to the reduced driving force for the main flow and the enhancement of heat transfer due to the increased fluid temperature with less cooling from side wall. In the top plate, as the heat transfer by secondary flows are dominant, the variation of h^*_{top}'s are not very significant. But, when the H/R decreases from 0.47 to 0.38, the degradation of heat transfer by reduced driving force seems to be dominant. However, when the H/R decreases further to 0.28, it is regarded that the enhancement of heat transfer by the higher fluid temperature becomes dominant.

The inflection points resulting from the multi-cell flow do not appear noticeably by unlike the results of the bottom plate due to the very high heat transfer contribution of the secondary flows underneath the top plate. The heat transfer from the position near 0.625 to edge is reduced steeply due to the cooling effect of the side wall.

Fig. 8 exhibits the normalized angular heat transfer coefficients for the side wall (h^*_{side}) for three different aspect ratios (H/R). The closed circle, triangle and square symbols denote the experimental results of this study. The open pentagon and star symbols indicate the results of the previous study performed by the same research group [9]. In all cases, h^*_{side}'s decrease with the angle from the 90°, showing the development of the thermal boundary layer from the top along the side wall. When the aspect ratio decreases, the heat transfer is impaired as the decrease of the H/R weakens the driving force for the main flow. At the lower edge of the side wall, all the results decrease sharply due to the stagnant flows.

4.3.2. Influence of the thermal boundary condition on local heat transfer

Fig. 9 compares the normalized local heat transfer coefficients at the bottom plate (h^*_{bottom}) for H/R of 0.28 for two different extreme top plate conditions: isothermal or adiabatic. The top isothermal condition shows better heat transfer than the top adiabatic condition. However, the trends are similar. For top isothermal condition, the main flow and secondary flow coexist in the oxide layer as shown in Fig. 5. However, for top insulated condition, there is only the main flow without secondary flow. Therefore, for the top isothermal condition, the heat transfer to the bottom plate is enhanced due to the more active convection in the oxide layer.

Fig. 10 shows the normalized local heat transfer coefficients of the top plate (h^*_{top}) for H/R of 0.28 for two extreme bottom thermal boundary conditions. The measured results at the top plate show little influence of the bottom thermal boundary conditions as the heat transfers of the top plate are much larger than those of the bottom plate due to the secondary flows.

Fig. 11 shows the normalized angular heat transfer coefficients for the side wall (h^*_{side}) for $H/R = 0.28$ with top thermal boundary conditions of isothermal and adiabatic. The heat transfers of top adiabatic case are higher than those of top isothermal case as the uncooled flows for the top adiabatic case dump more heat to the side wall.

4.4. Comparison of upward heat ratios according to aspect ratios

Fig. 12 presents the ratios of upward heat to total heat (Q^*_{up}/Q^*_{tot}), which in the current mass transfer system are the measured electricity ratios. These were normalized to maintain the same volumetric decay heat in all cases. The experimental results for this study correspond to $0.28 \leq H/R \leq 0.47$ and the multi-cell flow is observed in the oxide layer. The other results for $H/R = 0.56$, 0.78 and 1 are the results of the earlier studies performed by the same research group. For large H/R, twin-cell flows are observed. In the twin-cell cases, the upward heat ratios increase with the decrease

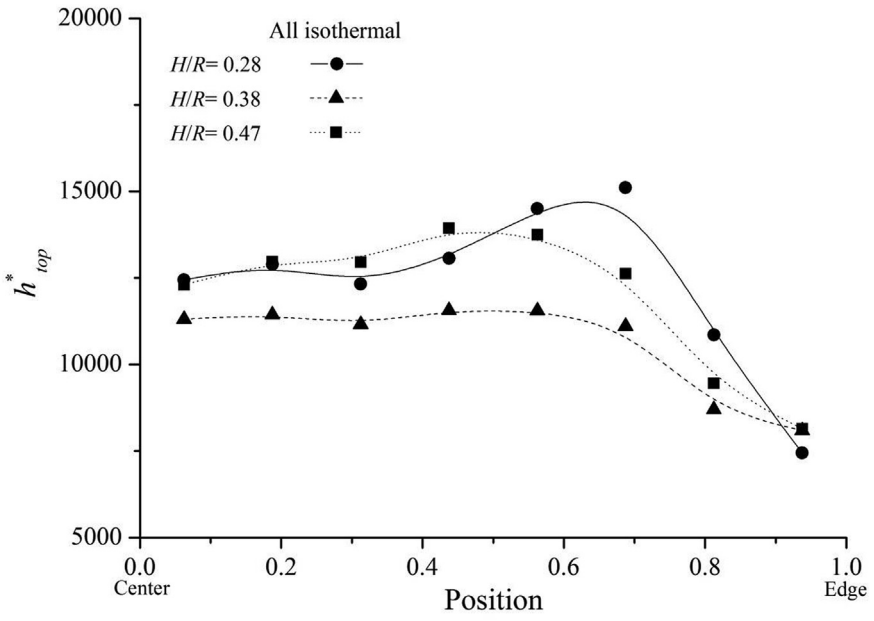

Fig. 7. Upward normalized heat transfer coefficients according to aspect ratios.

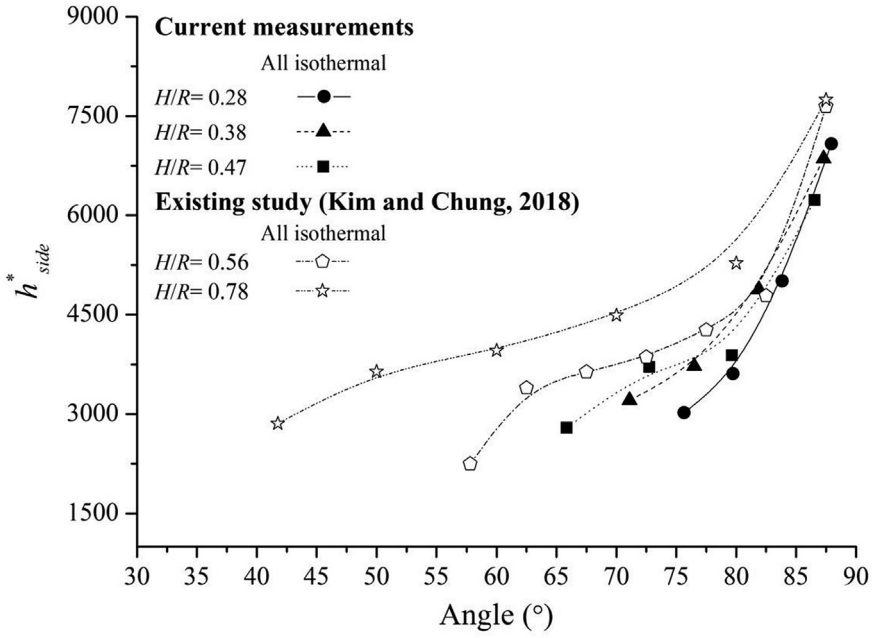

Fig. 8. Normalized heat transfer coefficients at the side wall according to aspect ratios.

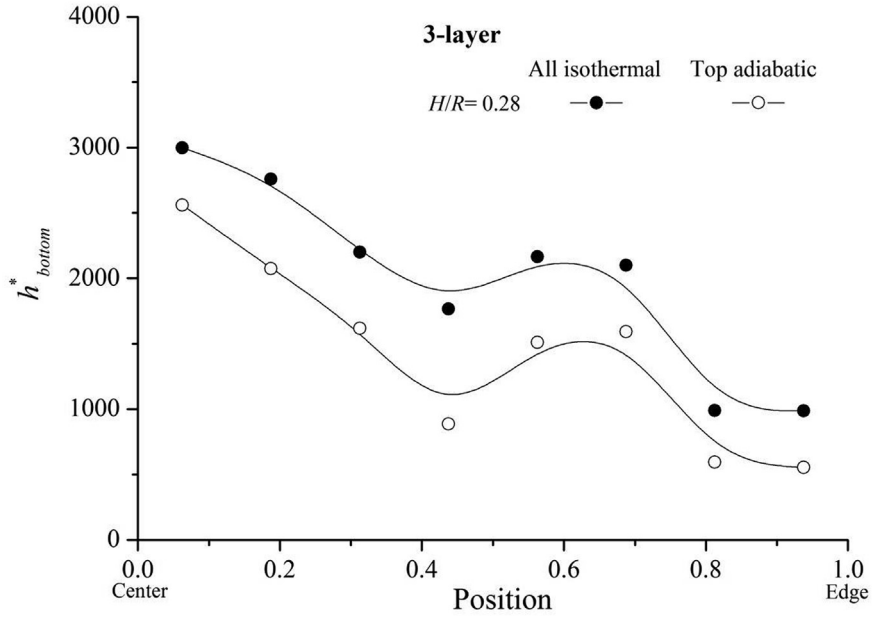

Fig. 9. Downward normalized heat transfer coefficient according to top plate cooling condition.

of H/R as the temperature of the upward plumes increases due to the shorter cooling length. However, in the multi-cell cases, the ratios are nearly constant regardless of the variation of the H/R as the multi-cell flows disperse the heat evenly.

5. Conclusions

The natural convection experiments of the oxide layer in the three-layer configuration were conducted simulating the IVR (In-Vessel Retention) situation at a hypothetical severe accident. The aspect ratios (H/R) and the thermal boundary conditions were varied with the aim of exploring the detailed phenomena of the multi-cell flow for small H/R's. In order to obtain large buoyance with compact test rig, the analogy between heat and mass transfer is utilized and the mass transfer experiments were performed replacing the heat transfer experiments. With the copper sulfate-sulfuric acid ($CuSO_4$–H_2SO_4) electroplating system, idealized thermal boundary conditions were imposed without heat leakage to the environment. The range of the high Ra'_H was 6.70×10^{10}–7.84×10^{12} and the Pr corresponding to Sc was 2014.

From the bottom plate heat transfer, we observed multi-cell flows in the shallow oxide layer whose H/R was equal or less than 0.47. The evidence of the multi-cell flow formation was the two inflection points of the heat transfer resulting from the ascending

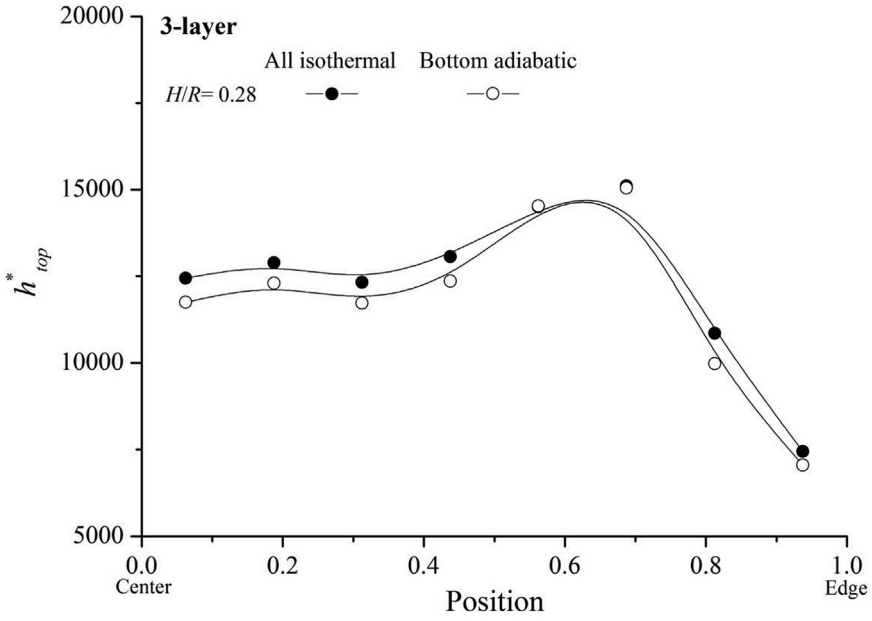

Fig. 10. Upward normalized heat transfer coefficient according to bottom plate cooling condition.

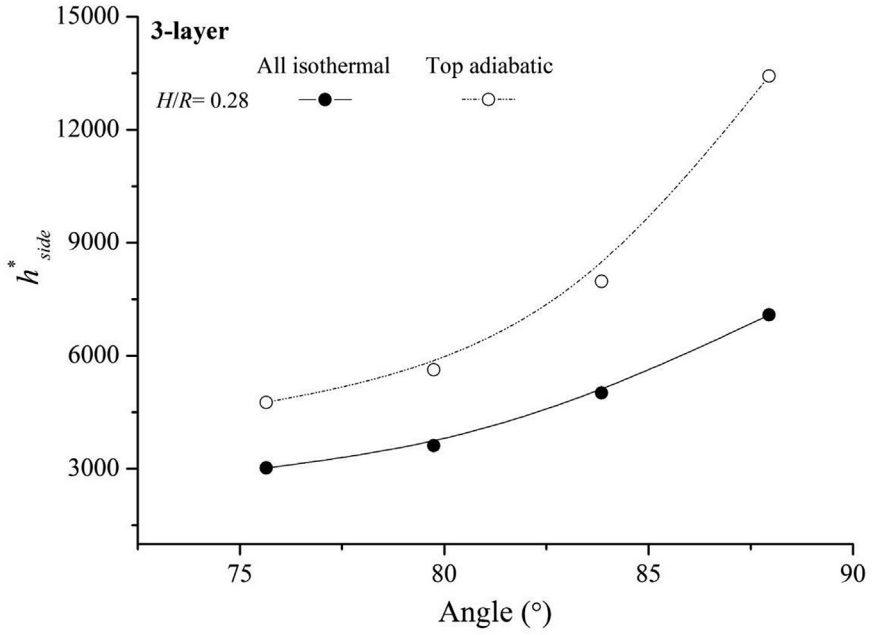

Fig. 11. Normalized heat transfer coefficient for side wall according to top plate cooling condition.

and descending plumes. Stagnant flows were observed at the corners formed by the side wall and the bottom.

The influences of the H/R on the local average heat transfer of the top and bottom plates were analyzed. There was the competition of two phenomena according to the decrease of H/R: the degradation of the heat transfer due to the reduced driving force for natural convection and the enhancement of heat transfer due to the less cooled, hotter flow moving toward top and bottom plates. When the H/R was reduced to 0.28 sufficiently, the latter was dominant in both of top and bottom plates.

The influences of the top and the bottom thermal boundary conditions on the local average heat transfers of the bottom and top plates were identified. The top boundary condition influenced the bottom heat transfer: The bottom heat transfer at top isothermal condition was larger than that at the top adiabatic condition. However, bottom boundary condition showed little influence on the top plate heat transfer.

The analysis for the normalized upward heat ratio (Q^*_{up}/Q^*_{tot}) showed that the decrease of H/R at the twin-cell condition caused the pronounced focusing effect as the upward flows had higher temperature due to the reduced cooling length. However, for very small H/R forming the multi-cell, the upward heat ratios were maintained about 80% as the multi-cell flow distributed the upward heat. Thus, we concluded that the focusing effect becomes similar for very small H/R less than 0.56.

The phenomenological analysis for the multi-cell flow in the

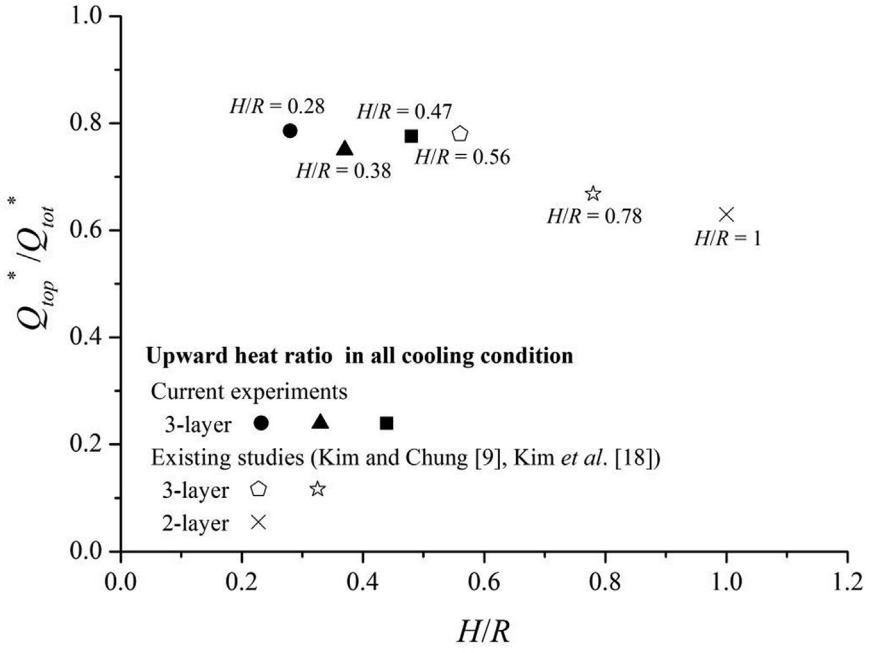

Fig. 12. Upward heat ratios for top plate varying aspect ratios.

oxide layer of small aspect ratio (H/R) was explored. This study can be used as a basis for development of the IVR-ERVC strategy. The originality of this study is confirming the influence of the multi-cell flow in the shallow oxide layer on the focusing effect.

Acknowledgment

This study was sponsored by the Ministry of Science and ICT (MSIT) through Nuclear Research & Development program grant funded by the National Research Foundation (NRF) (Grant code: 2017M2A8A4015283).

Appendix A. Supplementary data

Supplementary data to this article can be found online at https://doi.org/10.1016/j.net.2019.02.004.

References

[1] J.L. Rempe, et al., In-vessel retention of molten corium: lessons learned and outstanding issues, Nucl. Technol. 161 (2008) 210–267.
[2] S.D. Park, et al., Heat Removal Characteristics of IVR-ERVC Cooling System Using Gallium Liquid Metal, NURETH 16, Chicago IL, 2015.
[3] T.G. Theofanous, et al., In-vessel coolability and retention of a core melt, Nucl. Eng. Des. 169 (1997) 1–48.
[4] Y.J. Joe, et al., Development of assessment methodologies for corium coolability, Korea Inst. Nucl. Saf. (2015). KINS/HR-1410.
[5] R.J. Park, et al., Corium behavior in the lower plenum of the reactor vessel under IVR-ERVC condition: technical issues, Nucl. Eng. Technol. 44 (2012) 237–248.
[6] M. Fukasawa, S. Tamura, Thermodynamic analysis for molten corium stratification test MASCA with ionic liquid U-Zr-Fe-B-C-FPs database, J. Nucl. Sci. Technol. 44 (2007) 1210–1219.
[7] J. Wang, et al., In-Vessel Retention of Molten Core Debris for CAP1400, ICONE 18-29818, China, 2010.
[8] V. Barrachin, F. Defoort, Thermophysical properties of in-vessel corium: MASCA programme related results. Proceedings of MASCA Seminar 2004. Aix-en Provence, France, 2004.
[9] S.H. Kim, B.J. Chung, Mass transfer experiments on the natural convection heat transfer of the oxide pool in a three-layer configuration, Prog. Nucl. Energy 106 (2018) 11–19.
[10] F.A. Kulacki, A.A. Emara, Steady and transient thermal convection in a fluid layer with uniform volumetric energy sources, J. Fluid Mech. 83 (1977) 375–395.
[11] M.S. Sohal, L.J. Siefken, A Heat Transfer Model for a Stratified Corium-Metal Pool in the Lower Plenum of a Nuclear Reactor, Idaho National Engineering and Environmental Laboratory, 1999.
[12] Bonnet and Seiler, Thermal Hydraulic Phenomena in Corium Pools: the BALI Experiment, 7th International Conference on Nuclear Engineering, Tokyo, Japan, 1999.
[13] J.K. Lee, et al., Experimental study of natural convection heat transfer in a volumetrically heated semicircular pool, Ann. Nucl. Energy 73 (2014) 432–440.
[14] T.G. Theofanous, et al., The first results from the ACOPO experiment, Nucl. Eng. Des. 169 (1997) 49–57.
[15] F.J. Asfia, V.K. Dhir, An experimental study of natural convection in a volumetrically heated spherical pool bounded on top with a rigid wall, Nucl. Eng. Des. 163 (1996) 333–348.
[16] S.H. Kim, B.J. Chung, Heat load imposed on reactor vessels during in-vessel retention of core melts, Nucl. Eng. Des. 308 (2016) 1–8.
[17] H.K. Park, B.J. Chung, Mass transfer experiments for the heat load during in-vessel retention of core melt, Nucl. Eng. Technol. 48 (2016) 906–914.
[18] S.H. Kim, et al., Two- and three-dimensional experiments for oxide pool in in-vessel retention of core melts, Nucl. Eng. Technol. 49 (2017) 1405–1413.
[19] Sehgal, et al., Natural Convection Heat Transfer in a Stratified Melt Pool with Volumetric Heat Generation, 6th International Topical Meeting on Nuclear Reactor Thermal Hydraulics Operations and Safety (NUTHOS-6), Nara, Japan, 2004.
[20] S.H. Kim, et al., Natural convection of the oxide pool in a three-layer configuration of core melts, Nucl. Eng. Des. 317 (2017) 100–109.
[21] F.P. Incropera, D.P. Dewitt, Fundamentals of Heat and Mass Transfer, fifth ed., John Wiley & Sons Inc., New York, 2003, pp. 614–619.
[22] Bejan, Convection Heat Transfer, third ed., John Wiley & Sons, INC, New York, 2006, pp. 96–97, 173-179, 197-200, 512-516.
[23] E.J. Fenech, C.W. Tobias, Mass transfer by free convection at horizontal electrodes, Electrochim. Acta 2 (1960) 311–325.
[24] Y. Konishi, et al., Anodic dissolution phenomena accompanying supersaturation of copper sulfate along a vertical plane copper anode, Electrochim. Acta 48 (2003) 2615–2624.
[25] H.K. Park, et al., Variation in the angular heat flux of the oxide pool with Rayleigh number, Ann. Nucl. Energy 170 (2017) 128–135.
[26] W.G. Steele, H.W. Coleman, Experimental and Uncertainty Analysis for Engineers, second ed., John Wiley & Son, Canada, 1999.
[27] U. Steinberner, H.H. Reineke, Turbulent buoyancy convection heat transfer with internal heat sources, Int. Heat Transf. Conf. 6 (1978).
[28] M. Corcione, Effects of the thermal boundary conditions at the sidewalls upon natural convection in rectangular enclosures heated from below and cooled from above, Int. J. Therm. Sci. 42 (2003) 199–208.
[29] S. Ostrach, Natural convection in enclosures, J. Heat Transf.-Trans. ASME 110 (1988) 1175–1190.
[30] J.Y. Moon, B.J. Chung, Influence of Prandtl number, height and lateral cooling condition on laminar natural convection in a rectangular enclosure, Heat Mass Tran. (2018) 1–13 (online published).